This is the accepted manuscript made available via CHORUS. The article has been published as:

Large spin Hall effect in Si at room temperature

Paul C. Lou, Anand Katailiha, Ravindra G. Bhardwaj, Tonmoy Bhowmick, W. P. Beyermann, Roger K. Lake, and Sandeep Kumar

Phys. Rev. B **101**, 094435 — Published 31 March 2020

DOI: 10.1103/PhysRevB.101.094435

Large spin-Hall effect in Si at room temperature

Paul C. Lou[1], Anand Katailiha[1], Ravindra G Bhardwaj[1], Tonmoy Bhowmick[2], W.P. Beyermann[3], Roger K. Lake[2,4] and Sandeep Kumar[1,4*]

[1] Department of Mechanical Engineering, University of California, Riverside, CA 92521, USA

[2] Department of Electrical Engineering and Computer Science, University of California, Riverside, CA 92521, USA

[3] Department of Physics and Astronomy, University of California, Riverside, CA 92521, USA

[4] Materials Science and Engineering Program, University of California, Riverside, CA 92521, USA

Abstract

Silicon's weak intrinsic spin-orbit coupling and centrosymmetric crystal structure are a critical bottleneck to the development of Si spintronics, because they lead to an insignificant spin-Hall effect (spin current generation) and inverse spin-Hall effect (spin current detection). Here, we undertake current, magnetic field, crystallography dependent magnetoresistance and magneto-thermal transport measurements to study the spin transport behavior in freestanding Si thin films. We observe a large spin-Hall magnetoresistance in both p-Si and n-Si at room temperature and it is an order of magnitude larger than that of Pt. One explanation of the unexpectedly large and efficient spin-Hall effect is spin-phonon coupling instead of spin-orbit coupling. The macroscopic origin of the spin-phonon coupling can be large strain gradients that can exist in the freestanding Si films. This discovery in a light, earth abundant and centrosymmetric material opens a new path of strain engineering to achieve spin dependent properties in technologically highly-developed materials.

I. Introduction

The spin-Hall effect (SHE)[1,2] and its reciprocal is an efficient mechanism of generation and detection of spin current, which arises in materials with large intrinsic spin-orbit coupling (SOC). However, large SOC can also arise due to broken inversion symmetry. In case of centrosymmetric materials, the symmetry can be altered using inhomogeneous strain [2-6]. The broken symmetry in centrosymmetric materials will give rise to a flexoelectric polarization due to an inhomogeneous strain field as shown in Figure 1 (a)[7]. Recently, the flexoelectric effect[8-11] due to a strain gradient has been experimentally observed in centrosymmetric Si[12], which provides a foundation for this study. Based on the flexoelectric coefficient reported for Si[13], the strain and strain gradient mediated Rashba Dresselhaus SOC may lead to SHE in Si with a magnitude similar to that of GaAs (Supplementary information-A[14] and see, also, references [3,9,13,15-20] therein). Traditionally, strain gradient experiments involve bending thin films on soft substrates[12]. Alternatively, a freestanding beam will buckle automatically due to residual stresses. The stresses and, as a consequence, the buckling can be controlled using thermal expansion. Within this framework, we perform experimental measurements of SHE in Si (p-doped and n-doped) free-standing thin films. Using spin-Hall magnetoresistance (SMR), magnetoresistance (MR) as a function of crystallographic direction and magneto-thermal transport measurements, we report an unexpectedly large SHE that is comparable to or larger than those found in Pt.

(Figure 1)

II. Experimental setup

Using standard micro/nanofabrication techniques (Supplementary information-B[14]), we fabricated a freestanding, multilayer thin film structure with a four-probe longitudinal resistance setup as shown in Figures 1 (b,c). The false color scanning electron micrograph in Figure 1 (c) shows the fabricated experimental device geometry[21,22]. The length and width of the suspended beam are 160 μm and 12 μm, respectively. The materials and thicknesses of the multilayer thin film are Pd (1 nm)/$Ni_{80}Fe_{20}$(25 nm)/MgO (1.8 nm)/p-Si (2 μm).

There are two contributions to the strain and strain gradient in a freestanding thin film, residual thermal expansion strain due to the thin film processing and buckling strain due to the

removal of the substrate. The strain profile in the specimen will be superposition of a uniform normal strain due to thermal expansion and a strain gradient due to buckling as shown in Figure 1 (b). Residual stresses in thin films on a substrate may cause strain gradients, but they are not controlled. However, the buckling of a freestanding thin film will change with an increase in applied current mediated by Joule heating. If strain is a primary driving mechanism, the spin transport behavior will change as a function of current. In an all-metal system, the OP-AMR and SMR were shown to be functions of temperature [23] with a cross-over occurring below room temperature. Thus, Joule heating can result in pure temperature effects combined with temperature driven strain effects.

To estimate the strain in the Si near the interface, we made a similar device with a longer 600 μm Si beam so that we could measure the buckling deformation (Supplementary Figure S1) and estimate the residual stresses (Supplementary information–C[14]). From high resolution transmission electron microscope (HRTEM) diffraction along <110> and <111> directions, we estimate 4% tensile strain near the interface as shown in Figure 1 (d) and Supplementary Figure S2. This calculated stress is less than the fracture stress of single crystal Si[24]. While the strain is estimated for very small region of the thin film, but symmetry of beam bending helps us in estimating the strain gradient. It is noted that the HRTEM sample preparation may release some of the stresses leading to underestimation of strain. The HRTEM image also shows the presence of a native oxide (~3.7 nm) in spite of Ar milling. However, the oxygen deficient native oxide will have dangling bonds and pin-holes that allow spin dependent electron tunneling and indirect exchange interactions required for spin transport studies. HRTEM imaging is complemented by energy-dispersive X-ray spectroscopy (EDS) elemental mapping, which shows absence of any Ni or Fe diffusion in Si layer as shown in Supplementary Figure S3 (Supplementary information – D[14]).

III. Results

A. SMR measurement in p-Si thin film

SMR is a widely used characterization technique to identify SHE[25-27]. For SMR characterization, an angle dependent magnetoresistance (ADMR) measurement is carried out on a bilayer specimen that consists of a ferromagnetic (FM) layer and a normal layer. In our case, the normal layer is the Si layer. If SHE exists in the Si layer, the spin current absorption and

reflection at the FM interface depends on the angle of the externally applied magnetic field. The spin absorption and reflection at the FM interface then modulates the longitudinal resistance of the Si through the inverse SHE. The SMR behavior is identified by field rotation in the yz-plane (field perpendicular to the direction of current) as shown in Figure 1 (b).

The $Ni_{80}Fe_{20}$ thin film exhibits an out of plane anisotropic magnetoresistance (OP-AMR)[28] in the yz-plane due to dimensional confinement. Hence, the total magnetoresistance (MR) of the multilayer film will be a superposition of SMR from the Si layer and OP-AMR from the $Ni_{80}Fe_{20}$ as shown in Figure 1 (e). The angular resistance modulation (in the yz-plane) due to OP-AMR and SMR can be written as,

$$R = R_0 + (\Delta R_{OP-AMR} - \Delta R_{SMR}) m_y^2 \ , \qquad (1)$$

where R_0 is the base resistance, ΔR_{OP-AMR} is the modulation in resistance due to OP-AMR, ΔR_{SMR} is modulation in resistance due to SMR, and m_y is the magnetic moment projection along the y-axis defined in Fig. 1 (b,c). Using ADMR measurements in the yz-plane, the SHE behavior can be distinguished from the OP-AMR contribution due to their opposite symmetries as shown in Figure 1 (e).

The ADMR measurements are performed at a constant magnetic field of 4 T and as a function of applied current from 100 μA to 2 mA as shown in Figure 2 (a). The p-Si layer in the suspended structure is oriented along the <110> direction. At 100 μA, we observe an ADMR behavior having a polarity similar to OP-AMR as shown in Figure 1 (e) and 2 (a). At 500 μA, the MR behavior is minimal and a further increase in current to 2 mA leads to a change in polarity that can be attributed to the contribution from SMR dominating the OP-AMR. Due to competition between OP-AMR and SMR, the measured ADMR values are small and are reaching the limit of instrumental resolution as observed in Figure 2 (a). However, the results presented in Figure 2 (a) are not artifact due to instrumental resolution since they are supported by further measurements presented in this study.

To ensure that observed behavior is due to interlayer spin dependent interactions, we measured the MR of the specimen as a function of magnetic field applied along y-axis and z-axis as shown in Supplementary Figure S4 and magnetic hysteresis measurement as shown in Supplementary Figure S5 (Supplementary information-E[14] and see, also, references [29-31]).

The measurement clearly shows a spin valve behavior due to spin dependent interactions across the layers in spite of thick oxide layer.

To demonstrate the competition between SMR and OP-AMR, the ADMR measurement is carried out by keeping the current constant at 900 μA while increasing the magnetic field from 1 T to 10 T, as shown in 2 (b). At low fields, the ADMR behavior displays polarity similar to SMR, indicating that magnitude of SMR is larger than OP-AMR. The ADMR is minimal at 6 T and changes polarity with further increase in strength of applied magnetic field to 10 T. The OP-AMR is a function of magnetic field due to magnon MR while SMR is not. The magnetic field dependence of the ADMR is consistent with the picture of the two competing mechanisms of OP-AMR and SMR. To further support our argument, we measured the MR as a function of magnetic field from 14 T to -14 T as shown in Supplementary Figure S6 (Supplementary information-E[14] and see, also, references [29-31]). The measurement shows a transition from SMR to OP-AMR behavior around 6 T, which supports ADMR measurement. This behavior arises due to diverging slopes of high field magnon MR [31] for field applied along y-axis and z-axis. Since the slope of magnon MR in z-axis is larger, it supports our assertion that interlayer spin dependent interactions are responsible for SMR symmetry observed in ADMR measurements.

The observed SMR behavior can be quantified using thickness dependent measurements. However, unlike a deposited thin film, a single crystal Si layer makes thickness dependent measurements difficult. For quantitative estimation of the SMR, we calculate the maximum amplitude of the ADMR at each current using a sine square curve fit. The $Ni_{80}Fe_{20}$ resistance ($\rho_{Ni_{80}Fe_{20}} = 5.43 \times 10^{-7}$ Ωm) is measured from a control specimen and the resistance ($\rho_{p-Si} = 5.25 \times 10^{-5}$ Ωm) of the p-Si layer is estimated using a parallel resistor model. This value is consistent with the bulk SOI wafer resistivity of 0.001 – 0.005 Ω cm. With these resistivity values, 56% of the current flows in the $Ni_{80}Fe_{20}$ layer and 44% flows in the p-Si layer. Then, we measured ADMR in a $Ni_{80}Fe_{20}$ control sample as shown in Supplementary Figure S7 to evaluate the OP-AMR contribution. The OP-AMR measurement in the $Ni_{80}Fe_{20}$ control specimen clearly shows that non-linear effects due to high field are not the cause of SMR like symmetry behavior in p-Si sample. We fabricated a second control sample with 25 nm of SiO_2 in between the $Ni_{80}Fe_{20}$ and p-Si layers. The ADMR measurement on this sample also displays OP-AMR

response as shown in Supplementary Figure S8. To further support our work, we fabricated a third control sample with $Ni_{80}Fe_{20}$ (25 nm) on a freestanding oxide membrane. This sample also exhibits OP-AMR response as shown in Supplementary Figure S9. These control experiments clearly show that the observed SMR behavior arises due to the p-Si layer (Supplementary Section F[14]). From OP-AMR measurements on a $Ni_{80}Fe_{20}$ control specimen, we estimate the OP-AMR to be 0.125% at 4 T for the multilayer structure. Using this value for the OP-AMR, the magnitude of the SMR is 1.15 x 10^{-3} at 1.25 mA. It is an order of magnitude larger than that of Pt[25], and it is of same order as the SMR reported in some topological insulators[32,33]. To approximate the spin-Hall angle (Θ_{SH}), we utilize the SMR equations for a bimetallic[26] structure (the full expression is given in Supplementary information-H[14] and see, also, reference [34]). For our geometry and materials, it simplifies to

$$\frac{\Delta R_{xx}^{SMR}}{R_{xx}^{0}} \approx -\Theta_{SH}^{2}\frac{\lambda_N}{d}\frac{2*tanh^{2}\left(\frac{d}{2\lambda_N}\right)}{(1+\xi)coth\left(\frac{d}{\lambda_N}\right)} \approx -\Theta_{SH}^{2}\frac{2\lambda_N}{(1+\xi)d} \quad . \qquad (2)$$

For the measured values of $\frac{\Delta R_{xx}^{SMR}}{R_{xx}^{0}} = 7.88 \times 10^{-4} - 0.00115$, a p-Si spin diffusion length of $\lambda_N = 310$ nm[35], a Si layer thickness of $d = 2$ μm, and a current shunting parameter $\xi = 1.21$, the spin Hall angle is Θ_{SH} = 0.075-0.096. This value is three orders of magnitude larger than Θ_{SH}=10^{-4} reported previously for p-Si[36] and it is of same order as the spin-Hall angle of Pt ($\Theta_{SH} = 0.055 - 0.1$) [25,37]. 310 nm is one of the largest values of spin diffusion length reported for p-Si, and it results in a lower bound on the spin-Hall angle. Shikoh et al. [38] reported a spin diffusion length of 148 nm in p-Si whereas Weng et al. [39] reported a value of 40 nm. Using these values increases the estimated spin-Hall angles to 0.26. Hence, the extracted values of the spin-Hall angle for p-Si in our samples can be in the range of 0.075-0.26. These values are two orders of magnitude larger than GaAs are not expected to arise due to strain gradient only (Supplementary information- A[14]). However, the strain may be the underlying cause of the large variance in reported spin-Hall angle values.

B. Piezoresistive effects in p-Si

Similar to SMR, the longitudinal resistance of the specimen (R_{xx}^{0}), estimated from ADMR measurements, is also a function of applied current, as shown in Figure 2 (c). The

resistance decreases as the applied electric current is increased from 100 μA to 1.25 mA, and then it increases after 1.25 mA. The Joule heating due to the current leads to an increase in the sample temperature, which consequently causes thermal expansion induced stresses. P-Si[40], $Ni_{80}Fe_{20}$, and the composite multilayer[30] have positive temperature coefficients of resistance (TCR).We measured the resistance of the specimen as a function of chamber temperature from 300 K to 350 K as shown in Supplementary Figure S10, which clearly shows an increase in resistance as a function of temperature. The rise in chamber temperature does not increase the buckling stresses significantly since the substrate is also expanding. In contrast, an increase in current causes thermal expansion of the sample structure only since the substrate (heat sink) temperature is not changing. Hence, the resistance of the multilayer thin film should not decrease due to Joule heating. However, thermal expansion induced compressive stresses along the Si <110> direction leads to a decrease in the resistance attributed to piezoresistance[41-43]. For the freestanding structure in this study, the decrease in resistance from piezoresistance is larger than the increase in resistance due to the temperature rise for applied currents less than 1.25 mA. From the parallel resistor model, we estimate that the electrical resistance of the p-Si layer changes from ~360.5 Ω to ~349.3 Ω. The bulk piezoresistance coefficient for p-Si <110> is 71.8×10^{-11} m^2/N[42,43] and it changes by a factor of ~0.4[42] for doping concentrations above 10^{19} cm^{-3}. Using the piezoresistance coefficients, we estimate the change in compressive stress due to 1.25 mA of heating current is ~107 MPa in addition to residual stresses prior to Joule heating. The change in compressive stress of 107 MPa is larger than the estimated buckling stress (~20 MPa) of the specimen, which will enhance the existing strain gradient due to residual stresses. This analysis shows that strain and strain gradient is the underlying reason for increase in the magnitude of SMR observed in the current dependent ADMR measurements shown in Figure 2 (a).

(Figure 2)

C. SMR measurement in n-Si thin film

We attribute the SMR behavior in p-Si to spatially varying strain. Hence, strain effects should be observed in n-Si specimens as well. To verify it, we fabricated a Pd (1 nm)/$Ni_{80}Fe_{20}$ (75 nm)/MgO (1.8 nm)/n-Si (2 μm) freestanding structure in the same 4-probe measurement geometry as shown in Fig. 1 (b,c). The thickness of the $Ni_{80}Fe_{20}$ layer is increased, since the n-Si

is more conductive ($\rho_{n-Si} = 1.94 \times 10^{-5}$ Ωm) than the p-Si. Thicker $Ni_{80}Fe_{20}$ thin films do not exhibit OP-AMR behavior leading to simplified SMR estimates. The n-Si layer in the free-standing structure is oriented along Si <110> similar to p-Si. ADMR measurements as a function of current from 250 μA to 3 mA were taken as shown in Supplementary Figure S11. The resistance of the specimen increases with increasing current contrary to that of the p-Si sample. The sign of the piezoresistance coefficient for n-Si is opposite to that of p-Si. Hence, the compressive stress leads to an increase in resistance in the n-Si due to the piezoresistive effect. The measured SMR is 0.192% and shows a small decrease when the applied current is increased as shown in Figure 2 (d) unlike the p-Si sample. The magnitude of SMR is approximately twice as large as that of p-Si, which itself is larger than that of Pt. Assuming a spin diffusion length of 2 μm[44] for n-Si, we calculate the spin Hall angle to be 0.119 (Supplementary information-H[14]), which is larger than the calculated spin-Hall angle for the p-Si sample. The SMR behavior as a function of current in n-Si suggests that the strain dependent behavior of the n-Si sample is different from p-Si sample. The residual stresses evolve during Si and SiO_2 etching and other processing steps. The $Ni_{80}Fe_{20}$ layer is three times thicker in case of n-Si and the resulting residual stresses in n-Si after processing could be sufficient for the observation of the SMR behavior. In addition, the thin film structure can buckle to have either a convex or concave curvature, which will give rise to different signs for the strain gradient. However, further change in stresses (strain) due to thermal expansion may be relatively small to cause a significant change in the SMR behavior in case of n-Si.

D. Crystallography dependent MR in p-Si

The next step is to understand the effect of a ~4% tensile strain near the interface. We performed density functional theory (DFT) calculations of the band structure of Si with an applied strain along <001> and <110> directions. (Supplementary information- I[14] and see, also, references [45-50]). The applied strain lifts the degeneracy of the valence band maxima resulting in a strain mediated valence band splitting. A 4% tensile strain applied along <001> direction leads to an energy splitting of 317 meV in the valence band as shown in Figure 3 (a) and for compressive strain, the splitting increases to 412 meV as shown in Supplementary Figure S12 (d). Similarly, along <110>, an applied 4% tensile or compressive strain leads to valence band splitting of ~520 meV or 600 meV respectively as shown in Figure 3 (b) and

Supplementary Figure S12 (a)-(b) respectively. Applied strain has a significantly larger effect on the valence bands than on the conduction bands as shown in Supplementary Figure S12 (c)-(d). The fact that the SMR in p-Si (n-Si) has a strong (weak) dependence on the current is consistent with the picture of the SMR driven by temperature-controlled strain.

From DFT simulations, we observed that the valence band splitting due to strain in the <110> direction is different from that due to strain in the <100> direction. The symmetry of <110> strained Si will be lower than the <100>strained Si[51], which will give rise to a crystallographic dependent behavior. To ascertain the crystallographic direction dependent behavior, we fabricated a set of $Ni_{80}Fe_{20}$ (25 nm) / MgO (1 nm) / p-Si (2μm) multilayer structures with the longitudinal direction of the Si layer lying along <110>, and at 15^o, 30^o and 45^o with respect to <110> as shown in Figure 3 (c). The negative MR for the Si channel oriented along <110> has two kinks due to changes in slope indicated by the arrows. The kink at higher magnetic field (~1.1 T) corresponds to the change in slope at the saturation magnetization (M_s). The kink at low field (~0.2 T) is not expected for a $Ni_{80}Fe_{20}$ thin film hard axis magnetization. This kink can only arise due to spin dependent tunneling across the oxide barrier. The low field kink disappears for measurement along <100> direction or at 45 degrees from <110>, which indicates the changes in the spin dependent interactions between the $Ni_{80}Fe_{20}$ and the Si layers. The negative MR behavior arises from polycrystalline $Ni_{80}Fe_{20}$ thin film. And, the observed correlation of the MR with the Si layer crystallographic direction will not arise if there are no spin dependent tunneling and interactions. This measurement gives additional proof that exchange interactions are taking place in spite of thick oxide layer (MgO and SiO_2). We have also demonstrated that the spin dependent interactions are function of crystallographic direction of p-Si layer.

(Figure 3)

IV. Discussion

There are various mechanisms that can give rise to SMR behavior in Si. From experimental transport measurements, we demonstrate that inhomogeneous strain is the macroscopic cause of the SMR response in n- and p-doped Si. Microscopically, inhomogeneous strain can be modeled as Rashba-Dresselhaus SOC (Supplementary information-A[14]), which

can give rise to SMR behavior. However, the spin-Hall angle is larger than the one expected according to flexoelectric coefficients (Supplementary information-A[14]). Alternatively, inhomogeneous strain will give rise to internal effective magnetic field, which arises due to coupling of electron spin to the off diagonal elements of crystallographic strain tensor as described by Crooker et al.[4] and can give rise to SHE but that can also not explain the large magnitude of SMR observed in this study.

Recently, Lou et al.[52] demonstrated spin-phonon interactions leading to a change in thermal conductivity in both p-Si and n-Si[21,22]. While the charge carriers in p- and n-doped Si are different, the thermal transport is phonon mediated in both cases. We speculate that spin dependent electron-phonon scattering may also give rise to the observed SMR behavior reported earlier. In order to uncover the mechanistic origin of the behavior, we measured the transverse spin-Nernst effect (SNE) in p-Si (Supplementary information- J[14] and see, also, references [53,54]). While the magneto-thermal transport measurement shows transverse SNE behavior in the measurements, experimental results are inconclusive as shown in Supplementary Figure S14. However, these measurements do indicate the existence of interlayer spin-phonon coupling.

In heavy metals, mechanistic reason for both SHE and SNE is large SOC[55]. However, that is not true for Si where thermal transport is mediated by phonons as opposed to charge carriers. Microscopically, spin dependent interactions with phonons cause transverse spin current or SHE during charge transport. And, an inverse microscopic behavior occurs during thermal transport where phonons have spin dependent interactions with charge carrier and give rise to transverse spin current or SNE. Hence, a strain mediated spin dependent coupling between phonon and charge carrier is proposed to be the microscopic mechanism for SHE observed in this study.

Conclusion

This study presents an experimental evidence of inhomogeneous strain mediated spin-phonon coupling in centrosymmetric non-magnetic material[56]. The spin-phonon coupling and resulting efficient spin to charge conversion may be applicable to all diamond cubic semiconductors (GaAs, Ge, InSb etc.) under inhomogeneous strain. Manufacturing processes for strain engineering already exist not only for Si but also for other semiconductors. Topological

behavior can also arise from the inhomogeneous strain fields, which may also open simple materials systems for topological materials research irrespective of intrinsic spin-orbit coupling. In addition to proposed experimental studies, theoretical models that describe the spin-phonon coupling in centrosymmetric materials and resulting behavior also need to be developed. This work provides a starting point for such future studies.

Author contributions

PCL, AK and RGB have equal contribution to this work. PCL carried out the SMR and SNE setup fabrication and did the SMR measurements. AK and RGB fabricated the crystallography device fabrication and contributed to all the measurements. TB carried out the DFT calculations. SK conceived the idea, designed the experiments, coordinated the project, supervised the experimental work, performed data analysis, and led manuscript preparation. RKL supervised the theory and computational work and analyzed the experimental data. SK, WPB and RKL wrote the manuscript. All the authors discussed and commented on the manuscript.

Acknowledgement

The fabrication of experimental devices was done at Center for Nanoscale Science and Engineering at UC Riverside. Electron microscopy sample preparation and imaging was done at the Central Facility for Advanced Microscopy and Microanalysis at UC Riverside. Theory and analysis was supported as part of Spins and Heat in Nanoscale Electronic Systems (SHINES) an Energy Frontier Research Center funded by the U.S. Department of Energy, Office of Science, Basic Energy Sciences under Award No. #DE-SC0012670. This work used the Extreme Science and Engineering Discovery Environment (XSEDE),[50] which is supported by National Science Foundation Grant No. ACI-1548562 and allocation ID TG-DMR130081.

Data availability

The data that support the findings of this study are available from the corresponding author upon reasonable request.

Competing interests

The authors declare no competing interests.

References

[1] J. Sinova, S. O. Valenzuela, J. Wunderlich, C. H. Back, and T. Jungwirth, Rev. Mod. Phys. **87**, 1213 (2015).

[2] Y. K. Kato, R. C. Myers, A. C. Gossard, and D. D. Awschalom, Science **306**, 1910 (2004).

[3] B. A. Bernevig and S.-C. Zhang, Physical Review B **72**, 115204 (2005).

[4] S. A. Crooker, M. Furis, X. Lou, C. Adelmann, D. L. Smith, C. J. Palmstrøm, and P. A. Crowell, Science **309**, 2191 (2005).

[5] D. Xiao, M.-C. Chang, and Q. Niu, Reviews of Modern Physics **82**, 1959 (2010).

[6] D. Xiao, J. Shi, D. P. Clougherty, and Q. Niu, Physical Review Letters **102**, 087602 (2009).

[7] Z. Wu, J. B. Neaton, and J. C. Grossman, Nano Letters **9**, 2418 (2009).

[8] P. Zubko, G. Catalan, and A. K. Tagantsev, Annual Review of Materials Research **43**, 387 (2013).

[9] N. T. D., M. Sheng, Y. Yao-Wen, P. P. K., and M. M. C., Advanced Materials **25**, 946 (2013).

[10] P. V. Yudin and A. K. Tagantsev, Nanotechnology **24**, 432001 (2013).

[11] A. P. Pyatakov, A. S. Sergeev, F. A. Mikailzade, and A. K. Zvezdin, Journal of Magnetism and Magnetic Materials **383**, 255 (2015).

[12] M.-M. Yang, D. J. Kim, and M. Alexe, Science (2018).

[13] A. Schiaffino, C. E. Dreyer, D. Vanderbilt, and M. Stengel, Physical Review B **99**, 085107 (2019).

[14] See supplementary materials at [URL] for sample fabrication, material characterization details, MR measurements, control samples experimental results. spin-Hall angle calculation, additional band structure calculations and transverse spin-Nernst effect measurement.

[15] A. Manchon, H. C. Koo, J. Nitta, S. M. Frolov, and R. A. Duine, Nat Mater **14**, 871 (2015).

[16] X. Zhang, Q. Liu, J.-W. Luo, A. J. Freeman, and A. Zunger, Nat Phys **10**, 387 (2014).

[17] B. M. Norman, C. J. Trowbridge, J. Stephens, A. C. Gossard, D. D. Awschalom, and V. Sih, Phys. Rev. B **82**, 081304 (2010).

[18] B. Bauer, J. Hubmann, M. Lohr, E. Reiger, D. Bougeard, and J. Zweck, Applied Physics Letters **104**, 211902 (2014).

[19] D. Lee and T. W. Noh, Philosophical Transactions of the Royal Society A: Mathematical, Physical and Engineering Sciences **370**, 4944 (2012).

[20] S. Das, B. Wang, T. R. Paudel, S. M. Park, E. Y. Tsymbal, L.-Q. Chen, D. Lee, and T. W. Noh, Nature Communications **10**, 537 (2019).

[21] P. C. Lou and S. Kumar, Journal of Magnetism and Magnetic Materials **452**, 129 (2018).

[22] P. C. Lou and S. Kumar, physica status solidi (b), 1700545, 1700545 (2017).

[23] K. L. Wong, L. Bi, M. Bao, Q. Wen, J. P. Chatelon, Y.-T. Lin, C. A. Ross, H. Zhang, and K. L. Wang, Appl. Phys. Lett. **105**, 232403 (2014).

[24] F. Ericson and J. Å. Schweitz, J. Appl. Phys. **68**, 5840 (1990).

[25] M. Althammer, S. Meyer, H. Nakayama, M. Schreier, S. Altmannshofer, M. Weiler *et al.*, Phys. Rev. B **87**, 224401 (2013).

[26] J. Kim, P. Sheng, S. Takahashi, S. Mitani, and M. Hayashi, Phys. Rev. Lett. **116**, 097201 (2016).

[27] Y.-T. Chen, S. Takahashi, H. Nakayama, M. Althammer, S. T. B. Goennenwein, E. Saitoh, and G. E. W. Bauer, Phys. Rev. B **87**, 144411 (2013).

[28] T. G. S. M. Rijks, S. K. J. Lenczowski, R. Coehoorn, and W. J. M. de Jonge, Phys. Rev. B **56**, 362 (1997).

[29] W. Y. Lee, B. C. Choi, J. Lee, C. C. Yao, Y. B. Xu, D. G. Hasko, and J. A. C. Bland, Applied Physics Letters **74**, 1609 (1999).

[30] P. C. Lou, W. P. Beyermann, and S. Kumar, J. Appl. Phys. **Accepted** (2017).

[31] A. O. Adeyeye, G. Lauhoff, J. A. C. Bland, C. Daboo, D. G. Hasko, and H. Ahmed, Applied Physics Letters **70**, 1046 (1997).

[32] Y. Lv, J. Kally, D. Zhang, J. S. Lee, M. Jamali, N. Samarth, and J.-P. Wang, Nature Communications **9**, 111 (2018).

[33] K. Yasuda, A. Tsukazaki, R. Yoshimi, K. S. Takahashi, M. Kawasaki, and Y. Tokura, Phys. Rev. Lett. **117**, 127202 (2016).

[34] S. Dubois, L. Piraux, J. M. George, K. Ounadjela, J. L. Duvail, and A. Fert, Phys. Rev. B **60**, 477 (1999).

[35] S. P. Dash, S. Sharma, R. S. Patel, M. P. de Jong, and R. Jansen, Nature **462**, 491 (2009).

[36] K. Ando and E. Saitoh, Nat Commun **3**, 629 (2012).

[37] E. Sagasta, Y. Omori, M. Isasa, M. Gradhand, L. E. Hueso, Y. Niimi, Y. C. Otani, and F. Casanova, Phys. Rev. B **94**, 060412 (2016).

[38] E. Shikoh, K. Ando, K. Kubo, E. Saitoh, T. Shinjo, and M. Shiraishi, Phys. Rev. Lett. **110**, 127201 (2013).

[39] Y.-C. Weng, C. T. Liang, and J. G. Lin, Appl. Phys. Lett. **115**, 232101 (2019).

[40] P. C. Lou and S. Kumar, Journal of Physics: Condensed Matter **30**, 145801 (2018).

[41] C. H. Cho, R. C. Jaeger, and J. C. Suhling, IEEE Sensors Journal **8**, 1455 (2008).

[42] Y. Kanda, IEEE Trans. Electron Devices **29**, 64 (1982).

[43] C. S. Smith, Phys. Rev. **94**, 42 (1954).

[44] S. Zhang, S. A. Dayeh, Y. Li, S. A. Crooker, D. L. Smith, and S. T. Picraux, Nano Letters **13**, 430 (2013).

[45] P. E. Blöchl, Phys. Rev. B **50**, 17953 (1994).

[46] M. Ernzerhof and G. E. Scuseria, The Journal of Chemical Physics **110**, 5029 (1999).

[47] J. P. Perdew, K. Burke, and M. Ernzerhof, Phys. Rev. Lett. **77**, 3865 (1996).

[48] G. Kresse and J. Hafner, Phys. Rev. B **48**, 13115 (1993).

[49] G. Kresse and J. Furthmüller, Phys. Rev. B **54**, 11169 (1996).

[50] S. Grimme, Journal of Computational Chemistry **27**, 1787 (2006).

[51] G. L. Bir and G. E. Pikus, (1974).

[52] P. C. Lou, L. de Sousa Oliveira, C. Tang, A. Greaney, and S. Kumar, Solid State Communications **283**, 37 (2018).

[53] A. D. Avery, M. R. Pufall, and B. L. Zink, Phys. Rev. Lett. **109**, 196602 (2012).

[54] M. Schmid, S. Srichandan, D. Meier, T. Kuschel, J. M. Schmalhorst, M. Vogel, G. Reiss, C. Strunk, and C. H. Back, Phys. Rev. Lett. **111**, 187201 (2013).

[55] P. Sheng, Y. Sakuraba, Y.-C. Lau, S. Takahashi, S. Mitani, and M. Hayashi, Science Advances **3** (2017).

[56] L. Zhang and Q. Niu, Phys. Rev. Lett. **112**, 085503 (2014).

List of Figures

Figure 1. Illustration of the test device, the effect of strain, and competing magnetoresistance effects. (a) Flexoelectric polarization due to a strain gradient. (b) Device schematic and experimental setup for angle dependent magnetoresistance measurements in the yz-plane. The strain gradient due to thermal expansion and buckling is also shown. C denotes compression and T denotes tension. (c) A false color SEM micrograph showing the representative experimental device with freestanding channel, (d) high resolution transmission electron micrograph showing the thin film structure at the Si interface and the estimated strain in <110> direction. (e) Expected symmetry behavior of the magnetoresistance corresponding to OP-AMR and SMR.

Figure 2. The magneto-transport characterization of Si thin film samples. The angle dependent magnetoresistance as a function of rotation in zy-plane for Pd/$Ni_{80}Fe_{20}$/MgO/p-Si thin film system aligned along <110> direction (a) as a function of current showing transition from weak OP-AMR behavior to SMR at higher currents and (b) as a function of magnetic field showing transition from SMR at low fields to AMR at higher fields. Large arrow indicates direction of current and magnetic field change. (c) the electrical resistance as a function of current at 300 K showing decrease attributed to piezoresistance in p-Si along <110> increasing compressive strain and (d) The angle dependent magnetoresistance as a function of rotation in zy-plane for Pd/$Ni_{80}Fe_{20}$/MgO/n-Si thin film system aligned along <110> direction showing SMR behavior as a function of current for an applied magnetic field of 3 T. .

Figure 3. Crystallographic behavior. (a) the band structure of Si for 4% tensile strain applied along <100> and inset showing the energy splitting at the peak of valence band, (b) the band structure of Si for 4% tensile strain applied along <110> and inset showing the energy splitting at the peak of valence band and (c) the magnetoresistance for an applied out of plane magnetic field for current applied along <110> direction or along the flat of the Si(100) wafer, at 15^o to the <110> direction, at 30^o to the <110> direction and along <100> direction. Arrows showing saturation magnetization and possible canted states and its transition as a function of orientation.

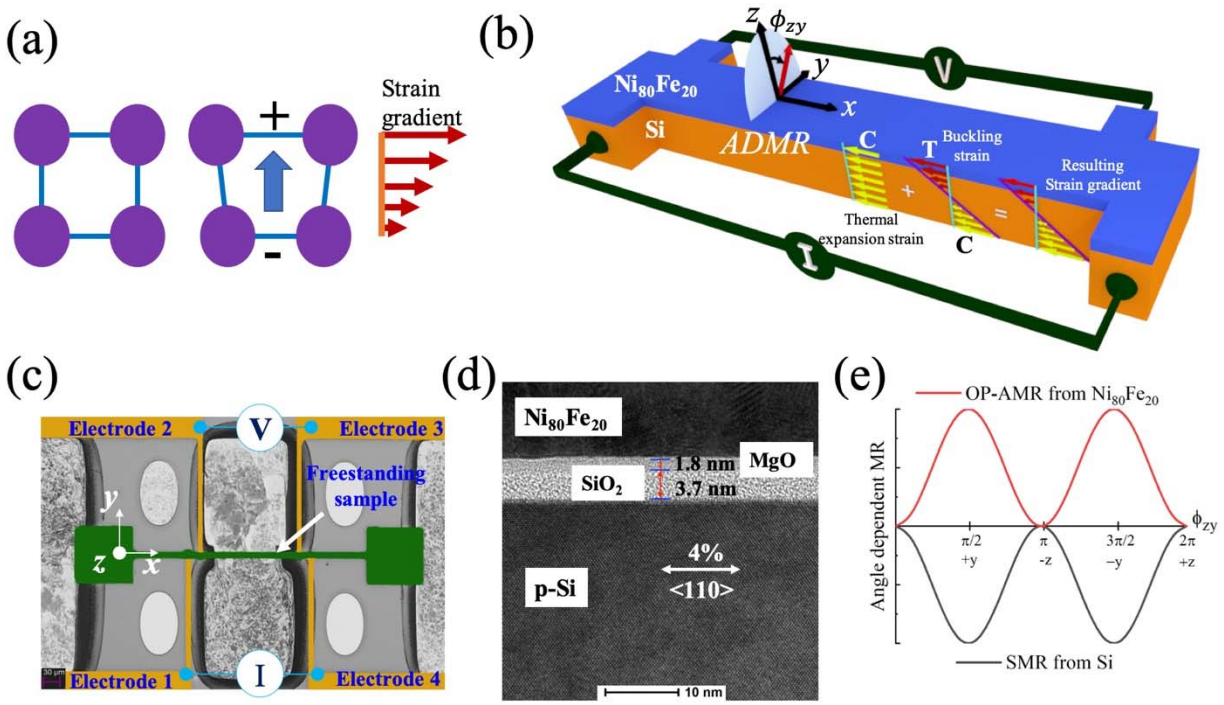
(a)
+
-
Strain gradient
(b)
z
ϕ_{zy}
y
x
$Ni_{80}Fe_{20}$
Si
ADMR
C
T
Buckling strain
Resulting Strain gradient
Thermal expansion strain
C
V
I
(c)
Electrode 2
V
Electrode 3
Freestanding sample
y
z
x
Electrode 1
I
Electrode 4
(d)
$Ni_{80}Fe_{20}$
SiO_2
1.8 nm
3.7 nm
MgO
4%
<110>
p-Si
10 nm
(e)
OP-AMR from $Ni_{80}Fe_{20}$
Angle dependent MR
ϕ_{zy}
π/2
+y
π
-z
3π/2
−y
2π
+z
SMR from Si

(Figure 1)

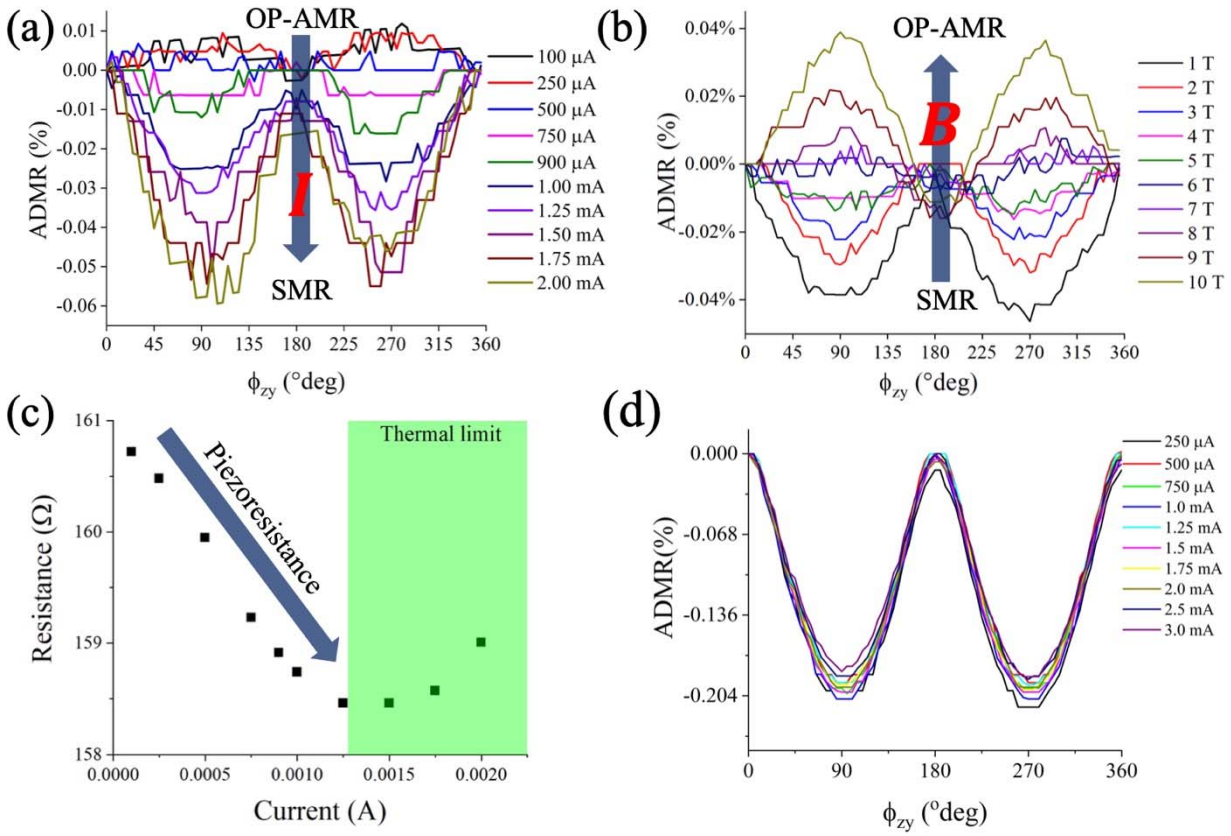
(a)
OP-AMR
SMR
I
ADMR (%)
ϕ_{zy} (°deg)
100 μA
250 μA
500 μA
750 μA
900 μA
1.00 mA
1.25 mA
1.50 mA
1.75 mA
2.00 mA
(b)
OP-AMR
SMR
B
ADMR (%)
ϕ_{zy} (°deg)
1 T
2 T
3 T
4 T
5 T
6 T
7 T
8 T
9 T
10 T
(c)
Thermal limit
Piezoresistance
Resistance (Ω)
Current (A)
(d)
ADMR(%)
ϕ_{zy} (°deg)
250 μA
500 μA
750 μA
1.0 mA
1.25 mA
1.5 mA
1.75 mA
2.0 mA
2.5 mA
3.0 mA

(Figure 2)

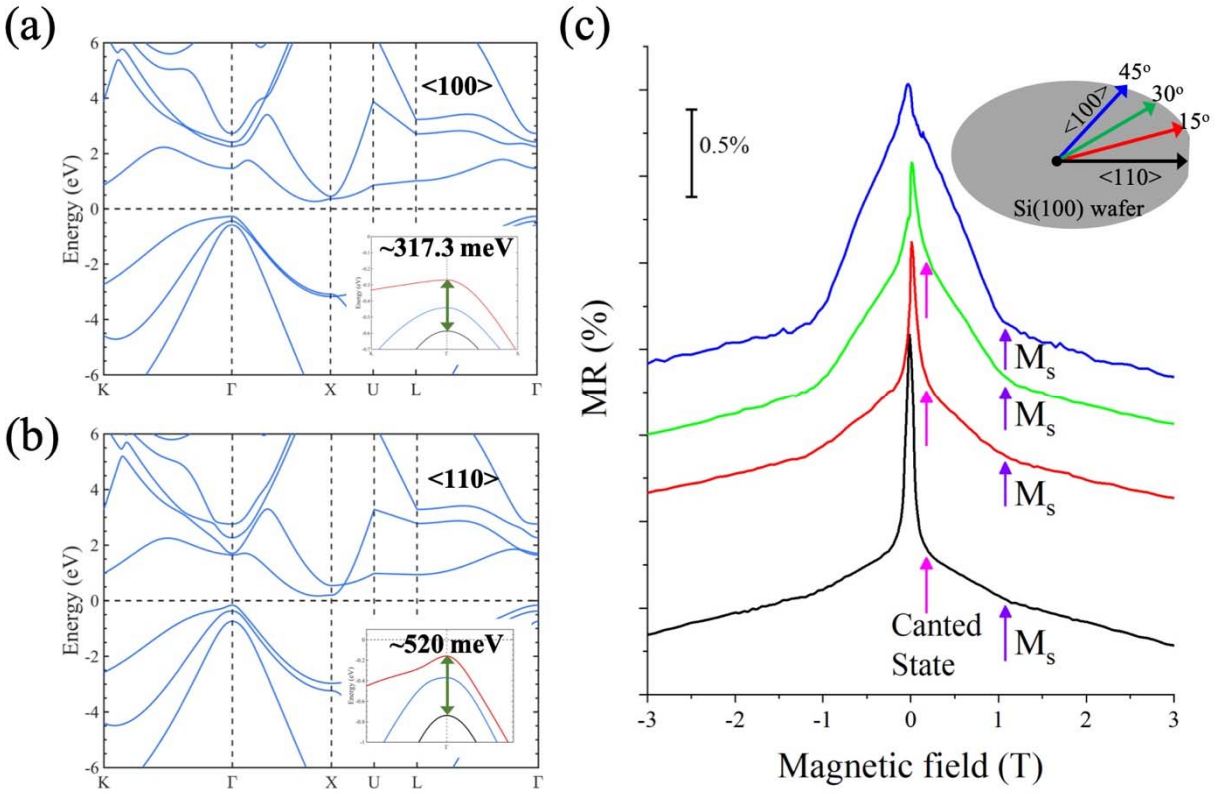
(a)
<100>
~317.3 meV
Energy (eV)
K
Γ
X
U
L
Γ
(b)
<110>
~520 meV
(c)
0.5%
45°
30°
15°
<100>
<110>
Si(100) wafer
MR (%)
M_s
Canted
State
Magnetic field (T)

(Figure 3)